Analytical Analysis and Performance Characterization of Brushless Doubly Fed Induction Machines Based on General Air-gap Field Modulation Theory

Peng Han[1*], *Ming Cheng*[2], *Xinkai Zhu*[3] *and Zhe Chen*[4]

(1. Ansys, Inc., San Jose, CA 95134, USA;

2. School of Electrical Engineering, Southeast University, Nanjing 210096, China;

3. Department of Electrical Engineering, North China Electric Power University, Baoding 071003, China;

4. Department of Energy Technology, Aalborg University, Aalborg 9220, Denmark)

Abstract: Air-gap magnetic field modulation has been widely observed in electric machines. In this study, we present an analytical analysis and performance characterization of brushless doubly fed induction machines (BDFIMs) fed by two independent converters from the perspective of air-gap field modulation. The spiral-loop winding is studied in detail as an example to show the generalized workflow that can also be used to analyze other short-circuited rotor winding types, such as nested-loop and multiphase double-layer windings. Magnetic field conversion factors are introduced to characterize the modulation behavior of special rotor windings and facilitate their comparison in terms of cross-coupling capability, average torque, and harmonic content of the air-gap flux density waveforms. The stator magnetomotive force (MMF), rotor MMF, and resultant air-gap MMF are considered, based on which the closed-form inductance formulas are derived, and the torque equation is obtained along with the optimal current angle for maximum torque operation by using the virtual work principle. The design equations are then developed for the initial sizing and geometry scaling of the BDFIMs. Transient finite element analysis and experimental measurements are performed to validate the analysis.

Keywords: AC machines, air gap, magnetic field, spatial harmonic, frequency domain, modulation, rotor windings

1 Introduction

Doubly fed induction machines (DFIMs) have been widely used as high-speed wind turbine generators because of their advantages of variable-speed constant-frequency operation, use of fractionally rated power converters, and independent controls of active and reactive power [1-2]. By supplying the two windings with two independent converters, it has been shown that the speed range can be doubled under the same DC bus voltage, which is attractive for applications in which a wide speed range is desired, such as electric vehicles and electric ship propulsion [3-4]. Brushes and slip rings are used to conduct AC currents through the rotor windings in slip-ring DFIMs, which leads to risks of failure and thus requires frequent maintenance.

The brush gears can be eliminated to enhance the reliability by moving the original rotor winding to the stator and adopting special rotor winding configurations, which leads to brushless DFIMs (BDFIMs). This study continues the research on wide-speed-range applications, focusing on the two-converter-based operation of BDFIMs following the pioneering work presented in Refs. [3, 5-6]. To enable the interaction between two stator windings through the intermediate action of the rotor while avoiding direct transformer coupling between stator windings, the pole pairs of stator winding 1 (SW1) and

Manuscript received April 5, 2021; revised May 21, 2021; accepted May 24, 2021. Date of publication September 30, 2021; date of current version August 11, 2021.

* Corresponding Author, E-mail: peng.han@uky.edu

Digital Object Identifier: 10.23919/CJEE.2021.000021

stator winding 2 (SW2) have to be different [7]. As a result, there are at least two dominating flux density harmonics in the air gap, as shown by the radial flux density waveform and its amplitude spectrum predicted from the two-dimensional (2-D) transient (time-stepping) finite element analysis (FEA) of a BDFIM fed by two independent converters, as shown in Fig. 1. This complicates the main magnetic circuit and its design analysis. It is worth noting that the two stator windings are termed as SW1 and SW2 in this study; these diff from the more commonly used terminologies — power winding and control winding — as we consider two-converter-based operation here. The BDFIM shown in Fig. 1 has an eight-pole SW1, a four-pole SW2, a rotor with six short-circuited coil nests, and three loops per nest.

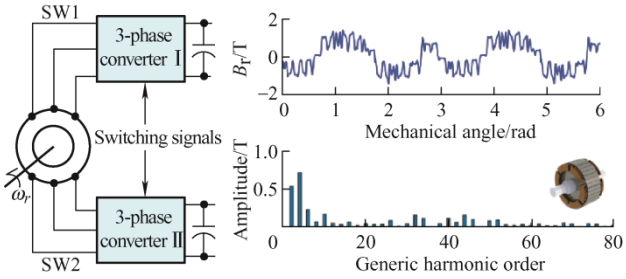

Fig. 1 Radial air-gap flux density waveform and its amplitude spectrum of a typical BDFIM supplied by two independent converters under a loaded condition from 2-D transient FEA

Existing research on BDFIMs relies heavily on coupled-circuit modeling or FEA and is mainly focused on wind power and ship shaft power generation applications, in which a fractionally rated back-to-back converter is used to supply the control winding, while the power winding is directly connected to the main grid or electric load. A full coupled-circuit model, which includes a number of position-dependent inductance terms under basic linear assumptions, has been developed for dynamic simulation and controller design with minimum loss of accuracy for the BDFIM with a nested-loop rotor [8]. A 2-D time-stepping FEA has also been performed to address core losses and magnetic saturation [9].

More recently, detailed FEAs have been conducted for various modes of operation of the BDFIM with a nested-loop rotor, showing the long transients before researching the steady state owing to the large time constant [10]. A computationally efficient magnetostatic FEA was proposed based on the space-time periodicity of the stator magnetomotive force (MMF) and used in optimization studies [11]. Owing to the nature of magnetostatic FEA, core losses have to be estimated using the modified Steinmetz equations, and torque ripple cannot be considered.

Detailed one-dimensional analytical magnetic field analysis, which may also be termed as harmonic analysis, has been performed on designs with nested-loop rotor windings with the goal of achieving a high accuracy comparable to FEA under linear assumptions [12-13]. The rotor MMF was analyzed in Ref. [14] with a focus on characterizing the harmonic contents of the air-gap magnetic field according to their pole pair numbers and rotational speeds without considering the amplitudes of these harmonics and their contributions to torque production.

These studies show advantages in the performance predictions of specific BDFIM designs as grid-connected or stand-alone generators, whereas they provide insufficient reference for the torque production mechanism and its design principle under two-converter-based operation. To the best of the authors' knowledge, design equations and procedures have only been discussed in Refs. [15-16] for BDFIMs with a back-to-back converter connected to control winding terminals. By omitting the magnetizing inductance and stator and rotor resistances, a power equation expressed by the specific electric loading and magnetic loading was developed based on the per phase equivalent circuit. It has been shown that the power equation depends on the machine operation and the turn ratio of the rotor winding. In addition, the definition of specific magnetic loading differs from that of conventional IMs or synchronous machines (SMs) because of the two dominating working spatial harmonics rotating in the air gap.

The design equations, analysis procedures, and steady-state performance of BDFIMs under two-converter-based operation have not been discussed before. In addition, there is a large design space for rotor winding configurations, even when the stator is given. The rotor winding can be of nested-loop type [8], spiral-loop type [17], and multiphase double-layer type [18]. The differences

among these winding configurations in terms of the cross-coupling capability and torque production, as well as how to take them into account during the early stage of machine design, need to be addressed before proceeding to a more detailed large-scale design optimization based on transient FEA, as exemplified in Ref. [19].

Air-gap field modulation theory was proposed in 2017 and has been demonstrated to be a powerful tool for analyzing the torque production mechanism, calculating inductances, and deriving torque equations for electric machines with features of multiple spatial harmonics and/or multiple ports [20]. The air-gap magnetic field modulation phenomenon in BDFIMs with a simplified loop rotor winding has been briefly analyzed in Refs. [21-23] based on the developed theory. This study extends the work published in conference papers [21-22] with a detailed theoretical analysis and enhanced experimental validation.

It should be noted that in this study we focus on the analytical analysis and basic performance characterization of brushless doubly fed induction machines, including the air-gap MMF distribution, inductance characteristics, and torque production. It is expected to lay a solid foundation for future studies on the torque-speed capability and efficiency map under various control schemes, which are currently beyond the scope of this study and will be reported in future publications.

The main contributions and novelties of this study are as follows.

(1) A detailed and unified theoretical analysis of the air-gap magnetic field of BDFIMs with closed-form equations for various rotor winding configurations and machine ratings and sizes is proposed. This is based on the general air-gap field modulation theory, starting from the stator MMFs, rotor MMFs, resultant air-gap MMF distribution, and inductance calculation to the torque production based on the principle of virtual work.

(2) A straightforward figure of merit called the magnetic field conversion factor is proposed. This can be used to characterize and compare various rotor winding configurations in terms of cross-coupling capability, average torque, and harmonic content of the air-gap flux density waveforms.

(3) The current angle, which is a function of the phase angles of the winding currents, positions of the stator winding axes, and rotor position is used to control the average torque. Based on this, the excitations for peak torque operation are determined and used in FEA simulations, eliminating the long searching process for the maximum torque operation point and enabling large-scale design optimization based on transient FEA.

(4) A full depiction of the steady-state performance of a 1.5-kW BDFIM with a spiral-loop rotor winding under a two-converter-based operation is presented based is on analytical-analysis-assisted transient FEA.

(5) Experimentally validated closed-form formulas for the estimation of machine inductances and torque per rotor volume for initial sizing and geometry scaling in the early machine design stage are derived.

The remainder of this paper is organized as follows: Section 2 presents a theoretical analysis of the air-gap magnetic field, inductance characteristics, and torque production in BDFIMs with various short-circuited rotor windings in a unified manner, revealing its operating principle from the perspective of air-gap field modulation. Section 3 derives the basic equations for the initial sizing and geometry scaling of BDFIMs with a specific design example. The performance characteristics of the design under two-converter-based operation are presented in Section 4. Section 5 presents the experimental validation of the inductance formulas and the proposed conversion factors. Finally, Section 6 concludes the paper.

2 Theoretical analysis

2.1 Methodology and basic assumptions

The basic relations in the spatial domain and spatial frequency domain offered by air-gap field modulation theory provide a new perspective for analyzing electric machines using closed-form analytical solutions following the signal flow of stator MMFs. To simplify the analysis, the following assumptions were made.

(1) The current in a single slot is located at the middle point of the slot opening.

(2) The air gap is uniform, and the slotting effect is taken into account by using Carter's factor.

(3) The permeability of the laminated steel is constant, and magnetic saturation is considered by using the saturation coefficient k_{sat}.

(4) The MMFs established by the stator windings are sinusoidal.

(5) The resistances and end turn leakage inductances of rotor windings are neglected in the analysis of doubly fed synchronous operation.

2.2 Stator MMF

Based on the coordinate system defined in Fig. 2 and neglecting harmonic terms, we can express the MMF created by SW1 as

$$\mathcal{F}_1^s(\phi,t)=F_1\cos\left[\left(p_1\phi-p_1\phi_{01}\right)-\left(\omega_1 t+\varphi_1\right)\right] \quad (1)$$

where F_1, the amplitude of the fundamental MMF created by SW1, is given by $F_1=(m_1/2)(2/\pi)\left(N_{ph}k_{w1}/p_1\right)$; p_1 is the number of pole pairs of SW1; N_{ph} is the number of turns in series per phase; k_{w1} is the fundamental winding function; m_1 is the number of phases of SW1; ϕ is the angular position along the air-gap periphery in the stationary reference frame; ϕ_{01} is the angle from the reference axis to the winding axis of SW1; ω_1 is the electrical angular frequency of SW1; t is time; and φ_1 is the initial phase of the SW1 current. The superscript s denotes the stationary reference frame and subscript 1 indicates SW1. The rotor windings can be of nested-loop type, spiral-loop type, and multiphase double-layer type. A spiral-loop rotor is shown in Fig. 2 as an example.

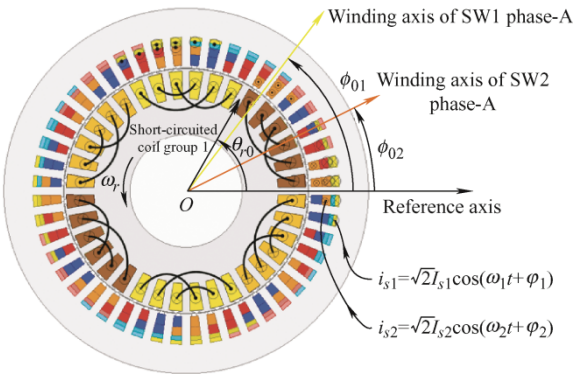

Fig. 2 Coordinate system and excitations used for the analysis of a BDFIM with short-circuited rotor windings

The MMF of SW1 in the rotor-speed reference frame is

$$\mathcal{F}_1^r(\underline{\phi},t)=F_1\cos\left[p_1\left(\underline{\phi}+\omega_r t+\theta_{r0}\right)-p_1\phi_{01}-\left(\omega_1 t+\varphi_1\right)\right] \quad (2)$$

where $\underline{\phi}$ is the angular position along the air-gap periphery in the rotor-speed reference frame, ω_r is the mechanical angular velocity of the rotor, θ_{r0} is the initial position of the rotor, and $\underline{\phi}=\phi-\omega_r t-\theta_{r0}$.

Similarly, the expressions for the MMF of SW2 can be obtained. The resultant stator MMF is the sum of those created by SW1 and SW2. In doubly fed synchronous operation (motoring or generating), the rotor speed is determined by the frequency and pole pairs of SW1 and SW2. There are two scenarios to maintain synchronous operation, that is, sum modulation and difference modulation [7, 12, 23-24].

(1) Sum modulation: When the rotor speed satisfies $\omega_r=(\omega_1+\omega_2)/(p_1+p_2)$, where ω_2 is the electrical angular frequency of SW2 and p_2 is the number of pole pairs of SW2, the number of antinodes of the resultant stator MMF wave in the air gap equals the summation of the two winding pole pairs, as shown in Fig. 3. This confirms the three-dimensional (3-D) visualizations of FEA results from the previous literature, for example, Refs. [13, 24], but with much reduced computational effort.

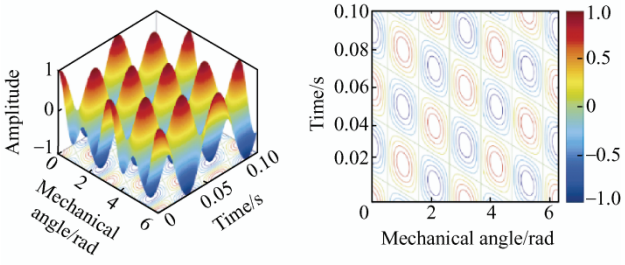

(a) 3-D view (b) Top view

Fig. 3 $\mathcal{F}_{1+2}^r(\underline{\phi},t)$ for sum modulation with $F_1=F_2$. $\omega_1=\omega_2=100\pi$ rad/s, and $\omega_r=100\pi/3$ rad/s

The color in the figure denotes the instantaneous value of the stator MMF. The stator MMF is no longer a traveling wave, as shown in conventional IMs and SMs. Instead, it exhibits features of proximate standing waves. Nodes (parts between the top and bottom sections) are points along the air-gap periphery where the resultant stator MMF wave has minimum amplitudes, such as $k\pi/6$, where k=1, 3, 5, 7, 9, and 11.

In contrast, the antinodes (the top and bottom parts) are located at $k\pi/6$, where k=0, 2, 4, 6, 8, and 10. At any instant of time, the stator MMF exhibits an approximate six-pole pattern.

It can be seen that, in the rotor-speed reference frame, the resultant stator MMF distribution is a function of both the angular position along the rotor peripheral and time and exhibits features of a proximate standing wave, as pointed out in Ref. [25].

(2) Difference modulation: In contrast, when the rotor speed is $\omega_r=(\omega_1+\omega_2)/|p_1-p_2|$, the number of antinodes or nodes of the resultant stator MMF wave in the air gap is two in this example, which means that the equivalent number of pole pairs is the difference between the two winding pole pairs, as shown in Fig. 4. Similar to the sum modulation, the resultant stator MMF distribution is also a function of both the angular position along the rotor peripheral and time. The difference lies in the contour patterns.

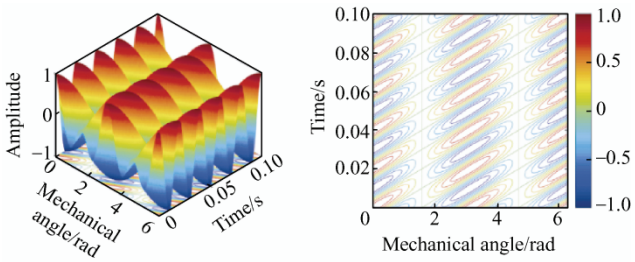

(a) 3-D view (b) Top view

Fig. 4 $\mathcal{F}_{1+2}^{r}(\underline{\phi},t)$ for difference modulation with F_1=F_2. ω_1=ω_2=100π rad/s, and ω_r=0 rad/s

The color in the figure denotes the instantaneous value of the stator MMF. The stator MMF is no longer a traveling wave, as in conventional IMs and SMs. Instead, it exhibits features of proximate standing waves. Nodes (parts between the top and bottom sections) are at $k\pi/2$, where k=1, 3. The antinodes (the top and bottom parts) are at $k\pi/2$, where k=0, 2. At any instant of time, the stator MMF in the rotor-speed reference frame exhibits an approximate two-pole pattern.

Unless specifically stated, this study focuses on the sum modulation, and the equations for difference modulation can be derived following the same procedure. By summing $\mathcal{F}_1^r(\underline{\phi},t)$ and $\mathcal{F}_2^r(\underline{\phi},t)$ and applying the sum-to-product identity, the resultant stator MMF produced by SW1 and SW2 in doubly fed motoring or generating operation can be written concisely as

$$\mathcal{F}_{1+2}^{r}(\underline{\phi},t)=\sqrt{F_1^2+F_2^2+2F_1F_2\cos(\alpha+\beta)}\times \cos\left(\omega_s t+(\alpha-\beta)/2-\vartheta\right) \tag{3}$$

where ω_s is the slip frequency, $\omega_s=\omega_1-p_1\omega_r=p_2\omega_r-\omega_2$, and

$$\vartheta=\operatorname{atan}2\left[(F_1+F_2)\cos\left(\frac{\alpha+\beta}{2}\right),(F_2-F_1)\sin\left(\frac{\alpha+\beta}{2}\right)\right] \tag{4}$$

with

$$\alpha=(\varphi_1+p_1\phi_{01})-p_1(\underline{\phi}+\theta_{r0}) \tag{5}$$

$$\beta=(\varphi_2+p_2\phi_{02})-p_2(\underline{\phi}+\theta_{r0}) \tag{6}$$

The time-variant stator MMF and its multi-harmonic nature complicate the analysis of BDFIMs with short-circuited rotor windings. The patterns of the resultant stator MMF with different MMF ratios are illustrated in Fig. 5 based on Eqs. (3)-(6), where F_1 and F_2 are the amplitudes of the fundamental MMFs produced by SW1 and SW2, respectively. It can be seen that, when only one stator winding is excited (which corresponds to the open-circuit operation of the machine), the stator MMF is a traveling wave with explicit pole numbers, as shown in Figs. 5a and 5j. When both stator windings are excited (i.e., the machine is operated with loads under two-converter-based operation), the resultant stator MMF pattern becomes a combination of traveling and standing waves [26], as shown in Figs. 5b-5i. No explicit pole numbers are observed.

The color in the figure denotes the instantaneous value of the stator MMF. When only one of the two stator windings is excited, the stator MMF is a traveling wave similar to those in conventional IMs and SMs, as shown in Figs. 5a and 5j. The stator MMF is no longer a traveling wave when both the stator windings are excited simultaneously. Instead, it exhibits features of proximate standing waves, which involve nodes (parts between the darkest sections) and antinodes (the darkest parts). Under two-converter-based operation, the ratio between F_1 and F_2 can be adjusted freely.

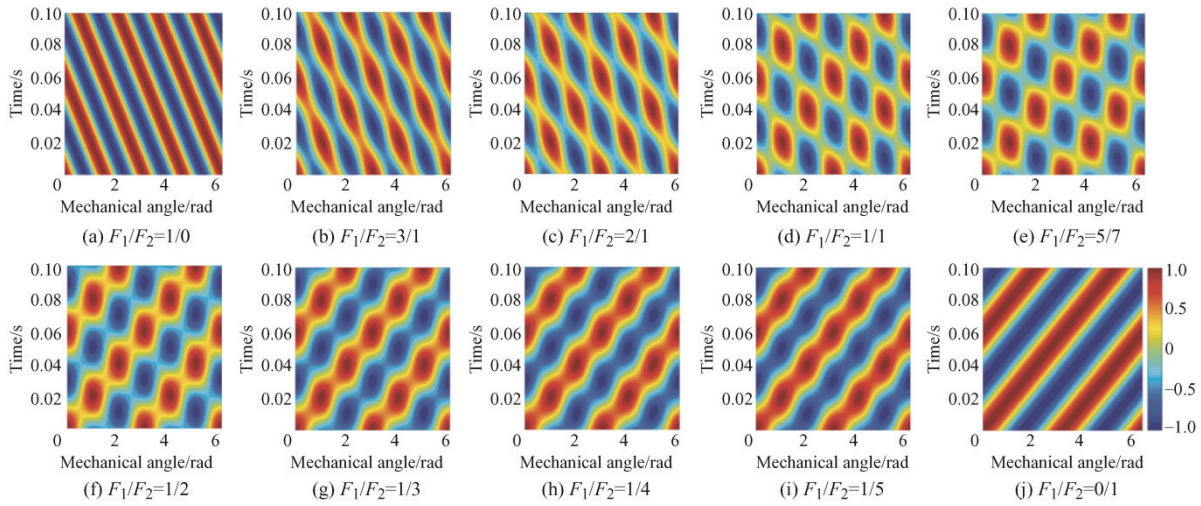

Fig. 5 Stator MMF patterns before considering the influence of rotor short-circuited coils

2.3 Rotor MMF for various rotor winding configurations

The presence of short-circuited rotor windings introduces additional MMFs, that is, the rotor MMF, into the air gap. The rotor MMF depends on the rotor winding current and winding function. The rotor MMF can be expressed as

$$\mathcal{F}_r^r\left(\underline{\phi},t\right)=\sum_{j=1}^{N_{SC}}W_j\left(\phi\right)i_{j(1)}+\sum_{j=1}^{N_{SC}}W_j\left(\phi\right)i_{j(2)} \tag{7}$$

where $W_j(\phi)$ and $i_{j(\phi)}$ are the winding function and current of the jth rotor winding, respectively; subscripts (1) and (2) denote the rotor currents induced by SW1 and SW2, respectively; N_{SC} is the number of short-circuited winding groups; and $N_{SC}=p_1+p_2$. There are S isolated short-circuited loops in each winding group. For spiral-loop windings and multiphase double-layer windings, S=1. The winding function of each short-circuited winding group, as shown in Fig. 6, can be calculated from the following definition

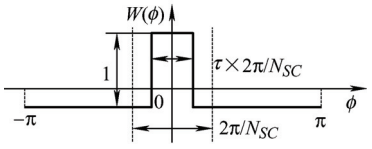

Fig. 6 Winding function of an individual coil with a span of $\tau\times2\pi/N_{SC}$

$$W_j\left(\phi\right)=T_j\left(\phi,\phi_0\right)-\frac{1}{2\pi}\int_0^{2\pi}T_j\left(\phi,\phi_0\right)\mathrm{d}\phi\qquad\phi\in\left[0,\ 2\pi\right] \tag{8}$$

where $T_j(\phi,\phi_0)$ is called the turn function and ϕ_0 is the lower bound of the integral, which does not appear in the winding function.

To determine the currents in the rotor short-circuited windings, one needs to look at the voltage equations of rotor short-circuited windings, which can be expressed in matrix form as

$$\boldsymbol{0}=\left[r_r\right]_{S\times S}\left[i_r\right]_{S\times1}+\frac{\mathrm{d}\left[\psi_r\right]_{S\times1}}{\mathrm{d}t} \tag{9}$$

where $[r_r]_{S\times S}$ is the resistance matrix, $[i_r]_{S\times1}$ is the rotor current vector, and $[\psi_r]_{S\times1}$ is the rotor flux linkage vector.

According to the assumption that the rotor resistances are negligible in a doubly fed synchronous operation, the rotor flux linkage vector in the steady state should be zero, which means that

$$\left[\psi_r\right]_{S\times1}=\left(\left[L_r\right]_{S\times S}-\left[L_{r-r}\right]_{S\times S}\right)\left[i_r\right]_{S\times1}+\left[\psi_{rs}\right]_{S\times1}=\boldsymbol{0} \tag{10}$$

where $[L_r]_{S\times S}$ is the group inductance matrix, which comprises the self- and mutual inductance of the loops within one winding group; $[L_{r\text{-}r}]_{S\times S}$ is the group-group mutual inductance matrix, which comprises the mutual inductance terms between loops of different groups; and $[\psi_{rs}]_{S\times1}$ is the flux linkage linked by a rotor winding group resulting from the air-gap magnetic field created by the stator windings.

The flux linkage linked by the ith loop, whose coil span is $\tau_i\times2\pi/N_{SC}$, can be calculated from

$$\left[\psi_{rs}\right]_i=\int_{(1-\tau_i)\pi/N_{SC}+(i-1)\times2\pi/N_{SC}}^{(1+\tau_i)\pi/N_{SC}+(i-1)\times2\pi/N_{SC}}B_1\left(\underline{\phi},t\right)l_{stk}r_g\mathrm{d}\underline{\phi}=$$
$$\frac{\mu_0r_gl_{stk}}{g_e}\left(\frac{2}{p_1}\right)\sin\left(\frac{\tau_ip_1\pi}{N_{SC}}\right)\times$$
$$\cos\left[\frac{\left(2i-1\right)p_1\pi}{N_{SC}}-\left(\omega_1-p_1\omega_r\right)t+p_1\theta_{r0}-\left(p_1\phi_{01}+\varphi_1\right)\right] \tag{11}$$

For the simplest case, where there are N_{SC} isolated short-circuited loops equally spaced on the rotor surface, the closed-form equation for the rotor

current can be obtained as

$$i_i(t) = -\sin\left(\frac{\tau p_1 \pi}{N_{SC}}\right) \Big/ \left(\frac{\tau p_1 \pi}{N_{SC}}\right) \times \cos\left[(2i-1)\frac{p_1\pi}{N_{SC}} - (\omega_1 - p_1\omega_r)t + p_1\theta_{r0} - (p_1\phi_{01} + \varphi_1)\right] \tag{12}$$

It can be seen that the amplitude of the rotor current depends only on the coil span and the pole combination of the stator windings once the rotor resistance is neglected. When the number of loops per group, S, is greater than one or a single short-circuited winding group has multiple slot conductors, the closed-form analytical solutions for the rotor current will become very complicated. In such cases, the rotor current expressions are obtained by symbolic computations using the Matlab Symbolic Math Toolbox.

By multiplying the rotor winding functions with rotor currents, the rotor MMF induced by a pure cosine stator MMF for a number of rotor winding configurations can be obtained, as shown in Fig. 7, together with the winding configuration of a single rotor winding group.

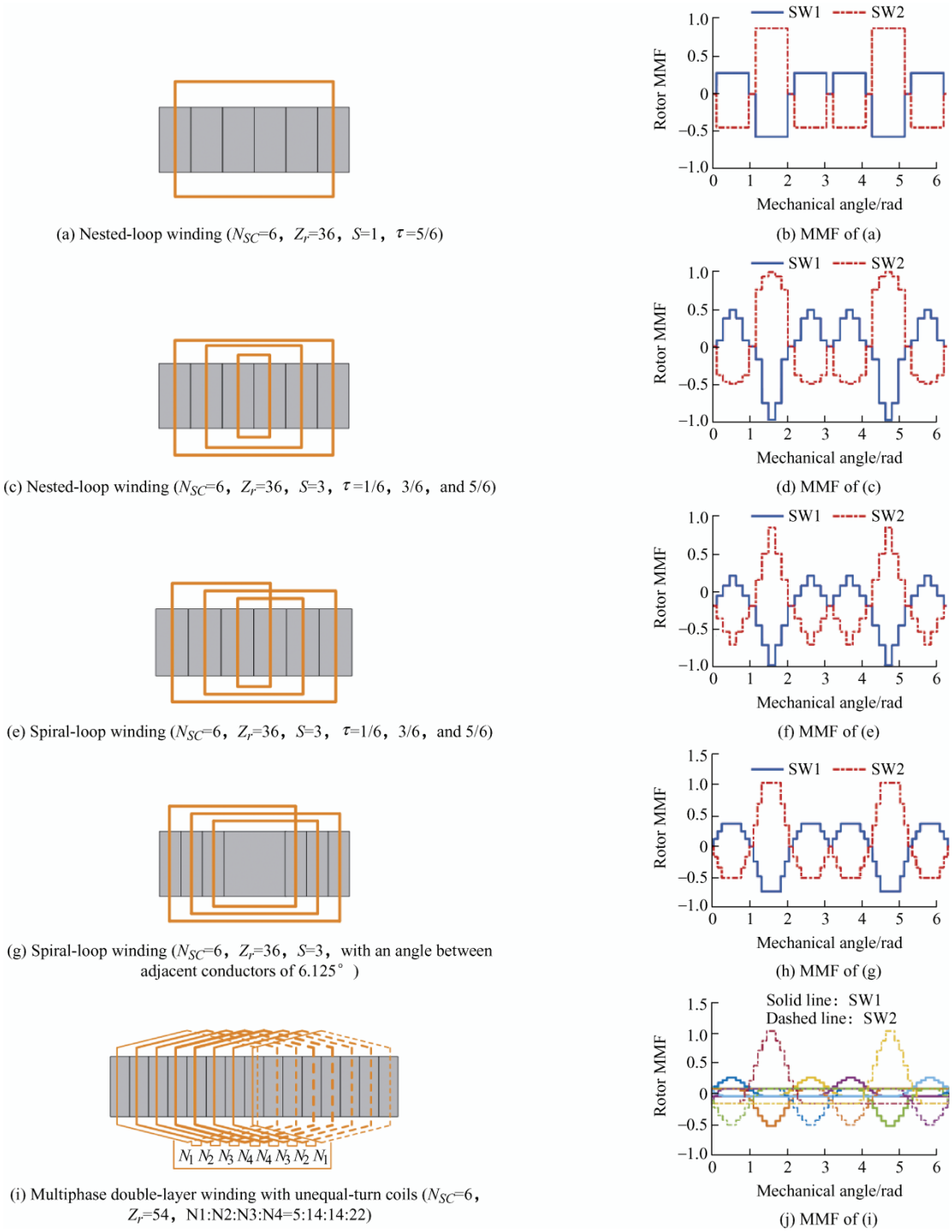

(a) Nested-loop winding (N_{SC}=6, Z_r=36, S=1, τ=5/6)

(b) MMF of (a)

(c) Nested-loop winding (N_{SC}=6, Z_r=36, S=3, τ=1/6, 3/6, and 5/6)

(d) MMF of (c)

(e) Spiral-loop winding (N_{SC}=6, Z_r=36, S=3, τ=1/6, 3/6, and 5/6)

(f) MMF of (e)

(g) Spiral-loop winding (N_{SC}=6, Z_r=36, S=3, with an angle between adjacent conductors of 6.125°)

(h) MMF of (g)

(i) Multiphase double-layer winding with unequal-turn coils (N_{SC}=6, Z_r=54, N1:N2:N3:N4=5:14:14:22)

(j) MMF of (i)

Fig. 7 Normalized MMF waveforms of various rotor windings. Only 1/6 of the rotor windings are shown in (a), (c), (e), (g), and (i)

It is worth noting that the presence of rotor resistance introduces an additional phase shift in the loop currents and the rotor MMF. Consequently, two asynchronous torque components produced by the interaction between the stator MMF and rotor MMF of the same pole pair numbers are introduced, which depend on the slip frequency and rotor resistance. The influence of the rotor resistance on the analytical analysis results is discussed in Section 4.

2.4 Resultant air-gap MMF

In general, the studied BDFIM is assumed to have a short-circuited rotor winding with N_{SC} winding groups and S loops per group. If the rotor rotates at a speed of ω_r, currents are induced in the rotor loops and an extra MMF distribution established by the rotor winding appears. By using the modulation operator of the short-circuited coils, $M(N_{SC})[\cdot]$, proposed in Ref. [20] and Ref. [23], the resultant air-gap MMF distribution can be expressed as

$$\begin{gathered} M\left(N_{SC}\right)\left[\mathcal{F}_{1+2}^{r}\left(\underline{\phi},t\right)\right]= \\ M\left(N_{SC}\right)\left[\mathcal{F}_{1}^{r}\left(\underline{\phi},t\right)\right]+M\left(N_{SC}\right)\left[\mathcal{F}_{2}^{r}\left(\underline{\phi},t\right)\right]= \\ \left[\mathcal{F}_{1}^{r}\left(\underline{\phi},t\right)+\sum_{j=1}^{N_{SC}}W_{j}\left(\phi\right)i_{j(1)}\right]+\left[\mathcal{F}_{2}^{r}\left(\underline{\phi},t\right)+\sum_{j=1}^{N_{SC}}W_{j}\left(\phi\right)i_{j(2)}\right] \end{gathered} \tag{13}$$

where $W_{ij}(\phi)$ is the winding function of the jth loop in the ith group and $M(N_{SC})[\cdot]$ is the modulation operator of the loop rotor with N_{SC} short-circuited winding groups.

Expanding Eq. (13) into the Fourier series, one can obtain the full spectrum of the resultant air-gap MMF distribution, which can be expressed as

$$M\left(N_{SC}\right)\left[\mathcal{F}_{1+2}^{r}\left(\underline{\phi},t\right)\right]=\boldsymbol{F}_{11}+\boldsymbol{F}_{21}+\boldsymbol{F}_{12}+\boldsymbol{F}_{22}+\left(\boldsymbol{R}_{1}+\boldsymbol{R}_{2}\right) \tag{14}$$

where $\boldsymbol{R}_1$ and $\boldsymbol{R}_2$ are remainders of lower amplitudes. $\boldsymbol{F}_{11}$, $\boldsymbol{F}_{21}$, $\boldsymbol{F}_{12}$, and $\boldsymbol{F}_{22}$ are dominating components, and they can be expressed as

$$\begin{cases} \boldsymbol{F}_{11}=F_{1}C_{p_1,p_1}\cos\left[\left(p_1\phi-\omega_1 t\right)-\left(p_1\phi_{01}+\varphi_1\right)\right] \\ \boldsymbol{F}_{21}=F_{2}C_{p_2,p_1}\cos\left[\left(p_1\phi-\omega_1 t\right)-\left(p_1\phi_{01}+\varphi_1\right)+\gamma\right] \\ \boldsymbol{F}_{12}=F_{1}C_{p_1,p_2}\cos\left[\left(p_2\phi-\omega_2 t\right)-\left(p_2\phi_{02}+\varphi_2\right)+\gamma\right] \\ \boldsymbol{F}_{22}=F_{2}C_{p_2,p_2}\cos\left[\left(p_2\phi-\omega_2 t\right)-\left(p_2\phi_{02}+\varphi_2\right)\right] \end{cases} \tag{15}$$

where $C_{x,y}$ (x,y=p_1,p_2) are the magnetic field conversion factors introduced by the modulation behavior of short-circuited rotor windings and γ is the current angle. The current angle can be expressed in terms of the positions of the winding axes, initial phases of the stator currents, and initial position of the rotor as follows

$$\gamma=\left(p_1\phi_{01}+\varphi_1\right)+\left(p_2\phi_{02}+\varphi_2\right)-N_{SC}\theta_{r0} \tag{16}$$

Eq. (14) and Eq. (15) show that there is always several field harmonics rotating at different speeds in the air gap, among which the field components with pole pairs of p_1 and p_2 are dominant.

$\boldsymbol{F}_{11}$ and $\boldsymbol{F}_{22}$ can be merged and expressed in the form of Eq. (3), and so can $\boldsymbol{F}_{21}$ and $\boldsymbol{F}_{12}$. By taking the simplest case as an example where there is only one loop per winding group, that is, S=1, and taking a loop span of $\tau\alpha_N$, where α_N=2π/N_{SC}, the conversion factors can be concisely expressed as

$$C_{p_i,p_i}=1-\tau\left[\sin\left(\tau\frac{p_i\alpha_N}{2}\right)\Big/\left(\tau\frac{p_i\alpha_N}{2}\right)\right]^2 \quad i=1,2 \tag{17}$$

$$C_{p_1,p_2}=\tau\left[\frac{\sin\left(\tau\dfrac{p_1\alpha_N}{2}\right)}{\left(\tau\dfrac{p_1\alpha_N}{2}\right)}\right]\left[\frac{\sin\left(\tau\dfrac{p_2\alpha_N}{2}\right)}{\left(\tau\dfrac{p_2\alpha_N}{2}\right)}\right] \tag{18}$$

With more complex rotor winding configurations, the symbolic expressions for the conversion factors can be derived by symbolic computations. By substituting specific numbers of pole pairs and coil spans into these expressions, the numerical values can be obtained. Some examples are listed in Tab. 1, demonstrating the universality of the proposed approach.

Tab. 1 Conversion factors of different rotor topologies derived from Fourier series expansion of Eq. (13)

Rotor topology	Winding pole pairs	Harmonic order													
		1	2	3	4	5	6	7	8	9	10	11	12	13	14
Nested-loop rotor (N_r=4, S=1, τ=1)	1	**0.189 4**	0	**0.270 2**	0	0.162 1	0	0.115 8	0	0.090 1	0	0.073 7	0	0.062 4	0
	3	**0.270 2**	0	**0.909 9**	0	0.054 0	0	0.038 6	0	0.030 0	0	0.024 6	0	0.020 8	0
Nested-loop rotor (N_r=6, S=1, τ=5/6)	2	0	**0.357 9**	0	**0.412 8**	0	0	0	0.071 7	0	0.157 5	0	0	0	0.020 8
	4	0	**0.412 8**	0	**0.734 7**	0	0	0	0.046 1	0	0.101 3	0	0	0	0.013 4
Nested-loop rotor (N_r=6, S=3)	2	0	**0.350 0**	0	**0.439 6**	0	0	0	0.017 3	0	0.111 5	0	0	0	0.022 1
	4	0	**0.439 6**	0	**0.642 6**	0	0	0	0.141 3	0	0.058 4	0	0	0	0.014 2
Spiral-loop rotor (N_r=6, slot pitch 10°)	2	0	**0.403 1**	0	**0.454 6**	0	0	0	0.120 9	0	0.027 1	0	0	0	0.015 8
	4	0	**0.454 6**	0	**0.653 8**	0	0	0	0.092 1	0	0.020 6	0	0	0	0.012 0
Spiral-loop rotor (N_r=6, slot pitch 6.125°)	2	0	**0.352 9**	0	**0.461 7**	0	0	0	0.044 5	0	0.061 0	0	0	0	0.050 4
	4	0	**0.461 7**	0	**0.670 6**	0	0	0	0.031 7	0	0.043 5	0	0	0	0.035 9
Six-phase unequal-turn design (N_r=6)	2	0	**0.213 7**	0	**0.402 4**	0	0	0	0.004 7	0	0.002 3	0	0	0	0.000 3
	4	0	**0.402 4**	0	**0.794 1**	0	0	0	0.002 4	0	0.001 2	0	0	0	0.000 2
Multibarrier rotor (N_r=6)	2	0	**0.293 3**	0	**0.413 5**	0	0	0	0.082 7	0	0.103 4	0	0	0	0.051 6
	4	0	**0.413 5**	0	**0.603 4**	0	0	0	0.206 8	—	0.059 1	0	0	0	0.082 7

In summary, the conversion factors are calculated in three steps using symbolic computational tools such as Wolfram Mathematica or Matlab Symbolic Math Toolbox.

Step 1: Apply a unit cosine stator MMF of p pole pairs whose expression is $\cos(p\phi-\omega t)$ on the air gap and assume that the rotor is cylindrical without short-circuited windings.

Step 2: Calculate the total electromotive force induced in each short-circuited coil, which can be an individual loop in nested-loop windings or spiral loops as a whole, and express them in vector format.

Step 3: Calculate the winding function of each short-circuited coil, based on which the self- and mutual inductances related to rotor windings can be obtained and incorporated into the inductance matrix.

Step 4: Calculate the current in each short-circuited coil and develop the rotor MMF based on the electromotive force vector and inductance matrix.

Step 5: Add the rotor MMF to the stator MMF $\cos(p\phi-\omega t)$ to obtain the resultant air-gap MMF distribution.

Step 6: Expand the resultant air-gap MMF into a Fourier series and extract the symbolic expressions for the coefficients of different spatial harmonic components.

The magnetic field conversion factors make it possible to compare different rotor winding configurations, including the reluctance rotor types [26]. For example, the spiral-loop rotor with six spiral loops and a slot pitch of 6.125° from the optimization in Ref. [17] can achieve the highest conversion factor between the eight-pole and four-pole air-gap field components. The six-phase unequal turn design in Ref. [18] had the lowest content of other spatial harmonics. In addition, the conversion factors are important to the inductance value and average torque, as will be shown in Sections 2.5 and 2.6.

2.5 Inductance characteristics

The first application of the MMF analysis was to estimate the machine inductances. The inductance between winding i and winding j can be obtained from

$$L_{ij}=k_{sat}\frac{\mu_0}{g_e}r_g l_{stk}\int_0^{2\pi}W_i(\phi)M(N_{SC})\left[W_j(\phi)\right]\mathrm{d}\phi \quad (19)$$

where $W_i(\phi)$ and $W_j(\phi)$ are the winding functions of the stator winding i and stator winding j, respectively. The self-inductance of the phase winding is independent of the rotor position and can be expressed as

$$L_{si}=k_{sat}C_{p_i,p_i}\frac{\mu_0\pi r_g l_{stk}}{g_e}\left[\frac{4}{\pi}\left(\frac{N_{ph\_si}k_{w1\_si}}{2p_i}\right)\right]^2 \quad i=1,2 \quad (20)$$

where N_{ph_s} is the number of turns in series per phase, k_{w1_s} is the fundamental winding factor, and subscripts 1 and 2 denote SW1 and SW2, respectively. The mutual inductance between the SW1 and SW2 phase-A windings is a cosine function of the rotor

position and can be expressed as

$$L_{1r2}^{\mathrm{AA}}=L_{2r1}^{\mathrm{AA}}=-k_{sat}C_{p_1,p_2}\frac{\mu_0\pi r_g l_{stk}}{g_e}\times \left[\left(\frac{4}{\pi}\right)^2\left(\frac{N_{ph\_s1}k_{w1\_s1}}{2p_1}\right)\left(\frac{N_{ph\_s2}k_{w1\_s2}}{2p_2}\right)\right]\times \cos\left(p_1\phi_{01}+p_2\phi_{02}-N_{SC}\theta_r\right) \quad (21)$$

Eq. (20) and Eq. (21) indicate that both the self-inductances and mutual inductance are reduced by the magnetic field conversion factors owing to the presence of the short-circuited rotor windings.

2.6 Torque production

Another application of the presented MMF analysis is to derive the torque equation and explain the torque production mechanism of the BDFIMs. Because the MMF drop or flux density distribution across the uniform air gap is known by applying the developed air-gap field modulation theory, the magnetic co-energy W_m' in the air gap can be obtained from

$$W_m'=\int_V\left(\frac{\mu_0}{g_e}\right)^2\frac{\left\{M\left(N_{SC}\right)\left[\mathcal{F}_{1+2}^r\left(\underline{\phi},t\right)\right]\right\}^2}{2\mu_0}\mathrm{d}V \quad (22)$$

where μ_0 is the permeability of vacuum, g_e is the effective air-gap length corrected by Carter's factor, and V is the air-gap volume.

The electromagnetic torque can be derived from magnetic co-energy using the virtual work principle. By keeping the current unchanged and creating a virtual displacement for the initial rotor position, the electromagnetic torque can be expressed as

$$T_{em}=\left.\frac{\partial W_m'}{\partial\theta_{r0}}\right|_{\text{current=const.}}=-\left(p_1+p_2\right)\frac{2\mu_0\pi r_g^3 l_{stk}}{g_e}\times \left(\frac{\overline{A}_1}{p_1}\right)\left(\frac{\overline{A}_2}{p_2}\right)\left(C_{p_1,p_1}+C_{p_2,p_2}\right)C_{p_1,p_2}\sin\gamma \quad (23)$$

where r_g is the air-gap radius, l_{stk} is the stack length, and $\overline{A}_1$ and $\overline{A}_2$ are the specific electric loadings of SW1 and SW2, respectively.

Eq. (23) shows that the synchronous electromagnetic torque in BDFIMs under two-converter-based operation is closely related to the pole pair combination and the specific electric loadings of both stator windings. For a given overall specific electric loading, the highest torque density is achieved by designs with a pole pair combination whose numbers of poles differ by 1 and equal allocation of specific electric loadings between two stator windings with an optimal $\gamma=\pi/2$.

3 Sizing equations with a design example

From Eq. (23), the torque density equation in terms of rotor volume, which is commonly used for the initial sizing of electric machines, can be obtained as follows

$$\frac{T_{em}}{\pi r_g^2 l_{stk}}=\left(p_1+p_2\right)\frac{2\mu_0 r_g}{g_e}k_{sat}\left(\frac{\overline{A}_1}{p_1}\right)\left(\frac{\overline{A}_2}{p_2}\right)\times \left(C_{p_1,p_1}+C_{p_2,p_2}\right)C_{p_1,p_2}\sin\gamma \quad (24)$$

where the specific electric loading of stator winding j is

$$\overline{A}_j=\frac{2m_j\left(N_{ph\_sj}k_{w1\_sj}I_{sj}\right)}{2\pi r_g}=\frac{p_jF_j}{\sqrt{2}r_g}\qquad j=1,2 \quad (25)$$

where m is the number of phases and I_s the rms value of the phase current. The specific magnetic loadings depend on the specific electric loading as follows

$$\overline{B}_{ij}=k_{sat}\frac{\sqrt{2}\mu_0}{g_e}\left(\frac{2}{\pi}\right)r_g\left(\frac{C_{p_i,p_j}}{p_j}\right)\overline{A}_j\qquad i,j=1,2 \quad (26)$$

Based on the design Eqs. (24)-(26), a prototype was designed whose specifications and key design parameters are listed in Tab. 2.

Tab. 2 Specifications and key design parameters of the 1.5-kW BDFIM prototype for two-converter-based operation

Parameter	Value
Stator outer/inner diameter/mm	182/127
DC bus voltage/V	600
Air-gap/stack length/mm	0.35/90
Number of stator/rotor slots	45/36
Rated torque/(N • m)	14.0(design value)/12.6 (achieved)
Rated speed/(r/min)	1 000 (frequency of SW1/2=50 Hz)
Pole pairs of SW1/2	4/2
Rotor winding configuration	Six equally spaced spiral loops
Turns in series per phase of SW1/SW2	510/255
Turns in series per spiral loop	15
Specific electric loading $\overline{A}_1$, $\overline{A}_2$/(kA/m)	18.13, 18.13
Power factor of SW1/SW2	0.53/0.56
Coefficient introduced by saturation, flux leakage, and rotor resistance	0.265
Torque per rotor volume/(kN • m/m^3)	44.70
Torque density/(kN • m/m^3)	21.53
Specific torque/(N • m/kg)	0.89
Efficiency(%)/coolant	76.0/Air

4 Performance chracteristics under two-converter-based operation predicted from analytical-analysis-assisted 2-D FEA

To demonstrate the performance characteristics of two-converter-based operation, 2-D magnetic transient FEA was performed for a full range of current angles and various frequency combinations following the derived current angle Eq. (16). The results are summarized in Figs. 8-9, respectively. It took 1 h and 37 min for a powerful workstation with an eight-core CPU and 128 GB of RAM to calculate each operating point. To reach the steady state, each operating point was calculated to have five full electric cycles with a low stator winding frequency and a total of 200 time steps.

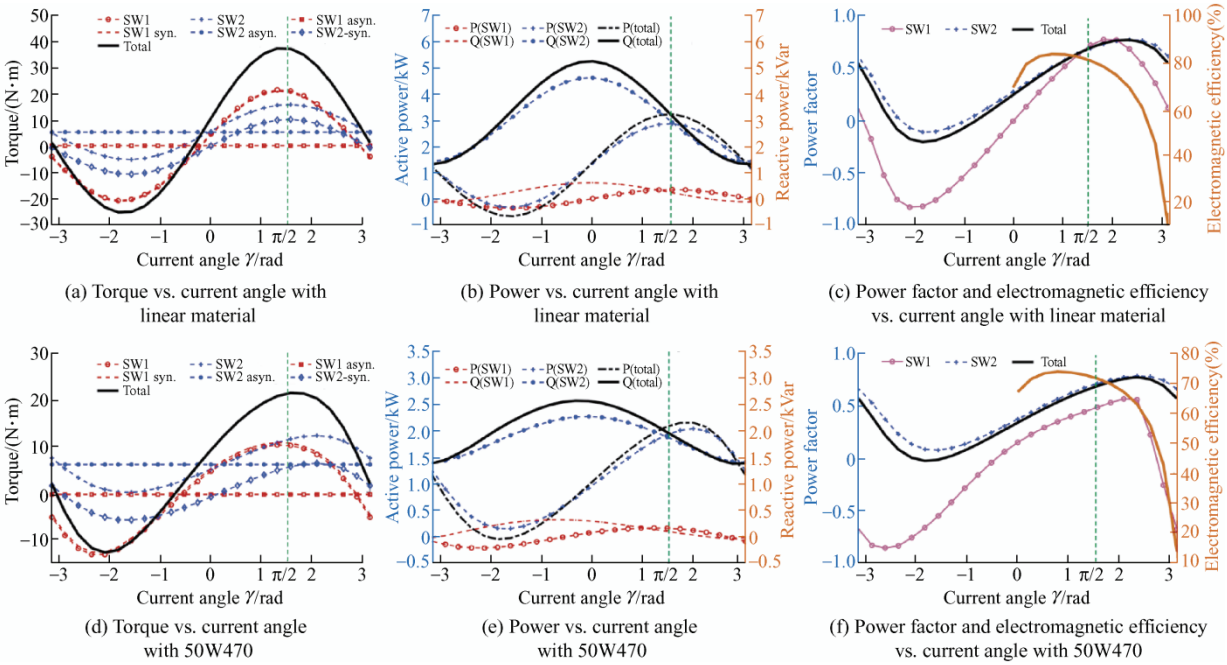

(a) Torque vs. current angle with linear material
(b) Power vs. current angle with linear material
(c) Power factor and electromagnetic efficiency vs. current angle with linear material
(d) Torque vs. current angle with 50W470
(e) Power vs. current angle with 50W470
(f) Power factor and electromagnetic efficiency vs. current angle with 50W470

Fig. 8 Performance of a 1.5-kW prototype at 600 r/min with linear and nonlinear lamination materials predicted from analytical-analysis-assisted 2-D FEA (SW1: 10 Hz, SW2: 50 Hz)

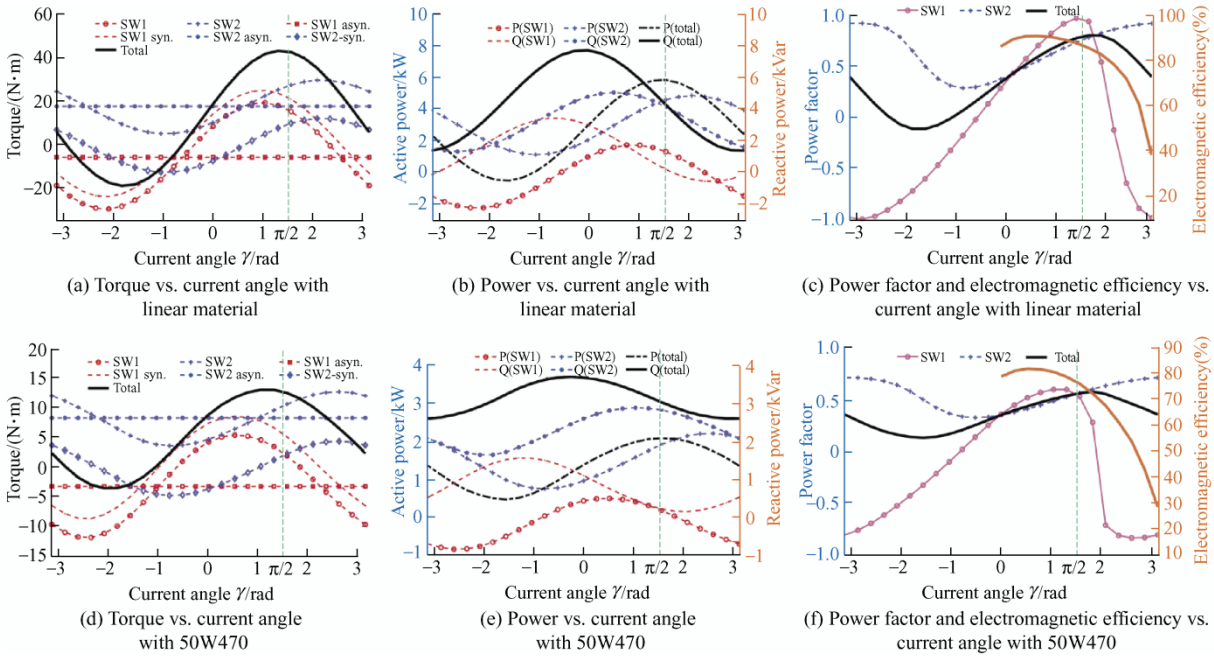

(a) Torque vs. current angle with linear material
(b) Power vs. current angle with linear material
(c) Power factor and electromagnetic efficiency vs. current angle with linear material
(d) Torque vs. current angle with 50W470
(e) Power vs. current angle with 50W470
(f) Power factor and electromagnetic efficiency vs. current angle with 50W470

Fig. 9 Performance of a 1.5-kW prototype at 1 000 r/min with linear and nonlinear lamination materials predicted from analytical-analysis-assisted 2-D FEA (SW1: 50 Hz, SW2: 50 Hz)

It should be noted that the current angle in Eq. (16) is the control variable for the calculation. This was not measured from the FEA results. By assigning the initial phase angles of the SW1 and SW2 currents and the initial rotor position for a given design, the current angle γ can vary from -180° to 180°.

With linear magnetic material, the torque curves at 600 r/min and 1 000 r/min are sine waves with positive DC offsets, as shown in Figs. 8a and 9a. Applying the derived optimal γ to FEA simulation settings makes it possible to avoid the time-consuming searching process for the maximum torque and to predict the peak torque by using one transient FEA simulation.

The maximum motoring torque occurs when the current angle is $\pi/2$, as indicated by Eq. (23) and Eq. (24). The breakdowns of the total electromagnetic torque were also included. The DC offsets denote the asynchronous torque components introduced by the rotor winding resistance. After the magnetic saturation is considered, the optimal current angle for maximum motoring torque deviates from $\pi/2$ but remains very close to this value, which can significantly reduce the searching range for the optimal current angle in large-scale design optimizations, as shown in Figs. 8d and 9d.

Under the linear condition, the active and reactive powers of each stator winding are sine and cosine waves, respectively, with positive offsets at 600 r/min. The total active and reactive powers exhibited similar trends. At 1 000 r/min, the active and reactive power curves of SW1 shifted to the left. In contrast, the active and reactive power curves of SW2 shifted to the right. As a result, the total active power still peaks at a current angle of $\pi/2$, and the maximum total reactive power still occurs at a current angle of zero. When the saturation effect is considered, the active power curves are distorted, and the maximum values occur at a current angle slightly greater than $\pi/2$ at both 600 r/min and 1 000 r/min.

One common observation from Figs. 8b and 8e is that the active and reactive powers of SW2, which is the fewer-pole-pair stator winding, are much greater than those of the more-pole-pair winding, that is, SW1. At 1 000 r/min, the proportions of active to reactive powers of SW1 increased, but they were still lower than those of SW2.

High power factors and electromagnetic efficiency can be achieved in a narrow current angle interval from 0 to 2 rad ($\approx 115^\circ$) regardless of the rotor speed and magnetic material type, indicating that the machine is very suitable for motoring operation in this range of current angle under two-converter-based operation.

It should be noted that, in Figs. 8c, 8f, 9c, and 9f, a positive power factor indicates a lagging power factor, and the machine absorbs active power from the supply. A negative value denotes a leading power factor. Under linear conditions, with some current angles (from $\approx -110^\circ$ to $\approx -60^\circ$), the machine as a whole can deliver some active power, but the amount is very low. The magnetic saturation effect almost eliminates the generating range under this new two-converter-based operation.

5 Experimental validation

To validate the presented theoretical analysis, a 1.5-kW BDFIM with a spiral-loop rotor designed in Section 3 was prototyped and tested. The control of two-converter-based operation has been implemented in Ref. [5] for the cascaded type, but further modifications are still needed for the BDFIM prototype.

The details of the motor components are presented in Fig. 10. The rotor has 36 slots and six separate spiral loops wound by 0.95-mm enameled copper magnet wires. Each spiral loop was wound loosely to have a bare copper slot fill factor of 0.335 to increase the rotor resistance and reveal the influence of rotor resistance. The four-pole winding, that is, SW2, was placed at the slot bottom because of its long end turns, and the eight-pole winding (SW1) was closer to the air gap. SW2 has 15 coils connected in series per phase, and each coil has 17 turns using 0.5-mm enameled copper magnet wires. SW1 has the same number of coils connected in series per phase, and each coil has 34 turns using the same magnet wire gauge. A large number of turns for each stator winding were used to achieve a rated phase voltage of 220 Vrms. Therefore, the DC resistances are relatively large, and the copper loss dominates the total loss.

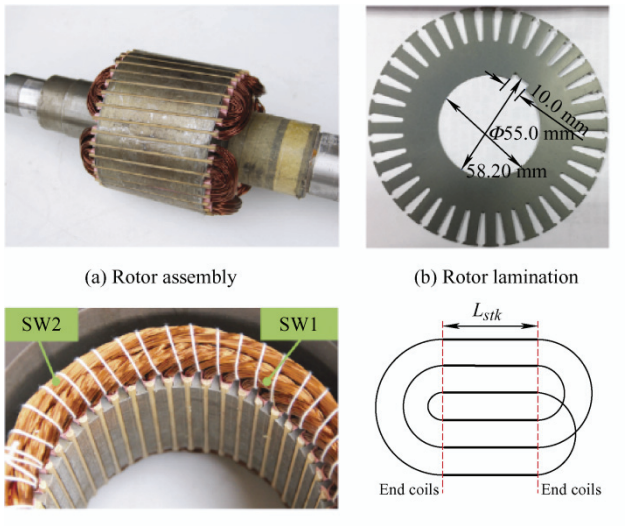

Fig. 10 Prototype of the BDFIM with spiral-loop rotor windings

The experimental setup for the inductance measurement, open-circuit testing, and future dynamic speed and torque control in Fig. 11 was tailored from a more general test rig for various brushless doubly fed machine types and various modes of operation, as shown in Ref. [23]. The two DC-AC converters were of the same rating and were used to supply SW1 and SW2 independently with variable voltage and frequency. A 5.5-kW permanent magnet SM was used as the load machine when the BDFIM under test was operated as a motor fed by two independent converters.

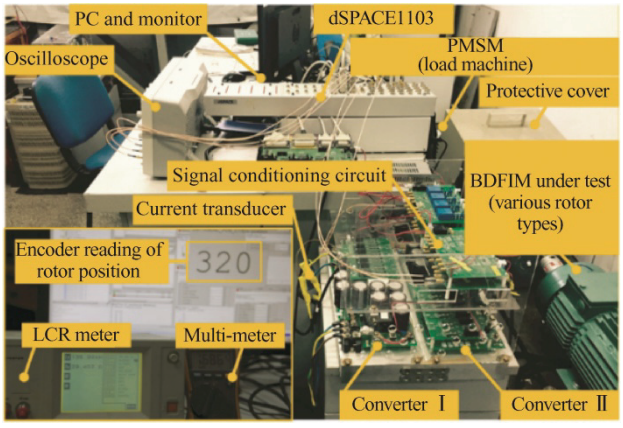

Fig. 11 Experimental setup for testing of the 1.5-kW BDFIM prototype with a spiral-loop rotor

Testing the BDFIM in both motoring and generating operations requires braking choppers, which need to be connected in parallel with the two independent DC buses. Detailed dynamic control and its effectiveness are beyond the scope of this study.

To validate the presented derivation for magnetic field conversion factors and the specific values for the rotor winding with six equally spaced spiral loops, the cross-coupling characteristic was measured in voltage mode, as shown in Fig. 12. The results generally agree well with the analytical predictions.

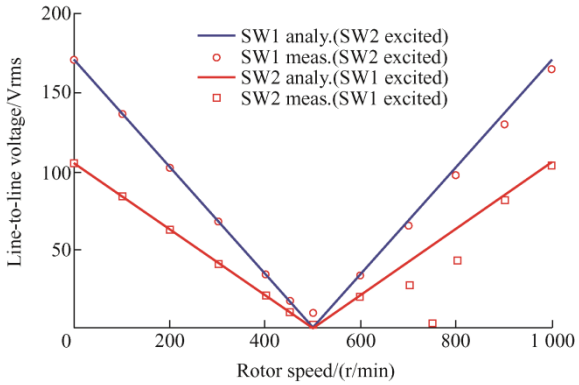

Fig. 12 Cross-coupling characteristic in voltage mode [excitation voltage (line-to-line): 190 Vrms, 50 Hz]

In this test, one of the stator windings was left open to measure the open-circuit voltage, while the other stator winding was supplied by a 190-Vrms (line-to-line value) and a 50-Hz three-phase voltage source in a wide speed range from 0 to 1 000 r/min. When SW1 was excited, the synchronous speed of the eight-pole field was 750 r/min. Therefore, there was no current induced in the rotor winding and no voltage at the terminals of SW2. This explains the drop in the measured voltage curve in the vicinity of 750 r/min, which cannot be captured by the analytical analysis.

To validate the inductance Eq. (20) and Eq. (21), the unsaturated inductances measured with an LCR meter were compared with those obtained from analytical predictions and FEA calculations, as shown in Fig. 13. In the experimental measurements, the influence of rotor short-circuited windings on the self- and mutual inductances related to SW1 and SW2 were considered. It can be seen that the self-inductances of SW1 and SW1-SW2 mutual inductances from the analytical prediction based on Eq. (20) and Eq. (21), the FE calculation, and measurements are all in very good agreement. Although there are some variations in the SW2 self-inductances, the differences are still within the 25% range.

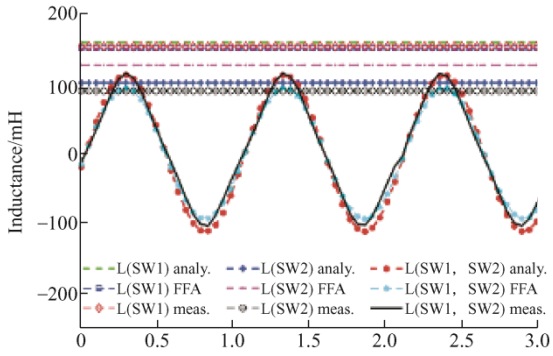

Fig. 13 Unsaturated inductances in the 1.5-kW prototype

6 Conclusions

A generalized theoretical analysis of BDFIMs with various short-circuited rotor winding types from the perspective of air-gap magnetic field modulation has been presented. The following have been shown.

(1) Both the stator and rotor MMFs have combined features of a traveling wave and a standing wave, that is, a proximate standing wave, and the MMF pattern varies with the ratio between the MMFs created by two stator windings under two-converter-based synchronous operation.

(2) The cross-coupling capability, which is essential to the torque production of this machine type and comparison with other rotor types, can be fully characterized by magnetic field conversion factors, based on which the concise closed-form expressions for inductances and torque density can be derived for parameter estimation, initial sizing, and geometry scaling.

(3) The maximum torque occurs at a current angle of $\pi/2$ under the linear assumption, and the optimal current angle deviates from $\pi/2$ slightly when the nonlinearity of the magnetic material is considered, which can be used to set the peak torque operating point in transient FEA simulations to effectively reduce the searching time.

(4) In addition to conventional use as a wind power or ship shaft power generator, BDFIMs are also very suitable for operation as a motor at a current angle close to $\pi/2$ to maximize the torque capability, power factor, and electromagnetic efficiency when supplied by two independent converters.

Experimental measurements of the open-circuit voltages at various speeds and unsaturated inductances performed on a 1.5-kW prototype with a spiral-loop rotor winding validate the analytical analysis. Static torque measurement, dynamic control of two-converter-based operation and its stability analysis, and large-scale design optimization based on transient FEA by incorporating the optimal angle derived in this study are underway and will be reported in the near future.

References

[1] M Cheng, Y Zhu. The state of the art of wind energy conversion systems and technologies: A review. *Energy Convers. Manag.*, 2014, 88: 332-347.

[2] H Li, Z Chen. Overview of different wind generator systems and their comparisons. *IET Renew. Power Gen.*, 2008, 2(2): 123-138.

[3] L Xu, Y Liu, X Wen. Comparison study of singly-fed electric machine with doubly-fed machine for EV/HEV applications. *Proc. Int. Conf. Electr. Mach. Syst.* (*ICEMS*), Beijing, China, 20-23 Aug. 2011.

[4] A Banerjee, M S Tomovich, S B Leeb, et al. Power converter sizing for a switched doubly fed machine propulsion drive. *IEEE Trans. Ind. Appl.*, 2015, 51(1): 248-258.

[5] P Han, M Cheng, Z Chen. Dual-electrical-port control of cascaded doubly-fed induction machine for EV/HEV applications. *IEEE Trans. Ind. Appl.*, 2017, 53(2): 1390-1398.

[6] R S Rebeiro, A M Knight. Two-converters-based synchronous operation and control of a brushless doubly fed reluctance machine. *IEEE Trans. Magn.*, 2018, 54(11): 8107205.

[7] P Han, M Cheng, S Ademi, et al. Brushless doubly-fed machines: Opportunities and challenges. *Chinese Journal of Electrical Engineering*, 2018, 4(2): 1-17.

[8] P C Roberts, T Long, R A McMahon, et al. Dynamic modelling of the brushless doubly fed machine. *IET Electr. Power Appl.*, 2013, 7(7): 544-556.

[9] A C Ferreira, S Williamson. Time-stepping finite-element analysis of brushless doubly fed machine taking iron loss and saturation into account. *IEEE Trans. Ind. Appl.*, 1999, 35(3): 583-588.

[10] H Gorginpour, H Oraee, R A McMahon. Performance description of brushless doubly-fed induction machine in its asynchronous and variable speed synchronous modes. *J. Electromag. Anal. Appl.*, 2011(3): 490-511.

[11] X Wang, T D Strous, D Lahaye, et al. Modeling and optimization of brushless doubly-fed induction machine using computationally efficient finite-element analysis. *IEEE Trans. Ind. Appl*., 2016, 52(6): 4525-4534.

[12] S Williamson, A C Ferreira, A K Wallace. Generalised theory of the brushless doubly-fed machine. Part 1: Analysis. *IEE Proc. - Electr. Power Appl.*, 1997, 144(2): 111-122.

[13] T D Strous, X Wang, H Polinder, et al. Brushless doubly fed induction machines: Magnetic field analysis. *IEEE Trans. Magn*., 2016, 52(11): 8108310.

[14] F Blázquez, C Veganzones, D Ramírez, et al. Characterization of the rotor magnetic field in a brushless doubly-fed induction machine. *IEEE Trans. Energy Convers*., 2009, 24(3): 599-607.

[15] R A McMahon, P C Roberts, X Wang, et al. Performance of BDFM as generator and motor. *IET Electr. Power Appl*., 2006, 153(2): 289-299.

[16] R A McMahon, M E Mathekga, X Wang, et al. Design considerations for the brushless doubly-fed (induction) machine. *IET Electr. Power Appl*., 2016(5): 394-402.

[17] H Gorginpour, B Jandaghi, H Oraee. A novel rotor configuration for brushless doubly-fed induction generator. *IET Electr. Power Appl*., 2013, 7(2): 106-115.

[18] F Xiong, X Wang. Design of a low-harmonic-content wound rotor for the brushless doubly fed generator. *IEEE Trans. Energy Convers*., 2014, 29(1): 158-168.

[19] V Rallabandi, P Han, J Wu, et al. Design optimization and comparison of direct-drive outer-rotor SRMs based on fast current profile estimation and transient FEA. *IEEE Trans. Ind. Appl.*, 2021, 57(1): 236-245.

[20] M Cheng, P Han, W Hua. General airgap field modulation theory for electrical machines. *IEEE Trans. Ind. Electron*., 2017, 64(8): 6063-6074.

[21] P Han, M Cheng, X Zhu, et al. Multifrequency spiral vector model for the brushless doubly-fed induction machine. *Proc. IEEE Int. Electr. Mach. Drives Conf.* (*IEMDC*), Miami, FL, USA, May 2017.

[22] P Han, M Cheng. Synthesis of airgap magnetic field modulation phenomena in electric machines. *Proc. IEEE Energy Convers. Congr. Expo*. (*ECCE*), Baltimore, MD, USA, Sept./Oct. 2019.

[23] M Cheng, P Han, Y Du, et al. A tutorial on general air-gap field modulation theory for electric machines. *IEEE J. Emerg. Sel. Top. Power Electron*., Jan. 2021, DOI: 10.1109/ JESTPE.2021.3055224.

[24] Y Cheng, B Yu, C Kan, et al. Design and performance study of a brushless doubly fed generator based on differential modulation. *IEEE Trans. Ind. Electron*., 2020, 67(12): 10024-10034.

[25] X Chen, X Wang. Proximate standing wave feature of magnetic field and its influence on the performance of wound rotor brushless doubly-fed machine. *IEEE Trans. Energy Convers*., 2017, 32(1): 296-308.

[26] P Han, J Zhang, M Cheng. Analytical analysis and performance characterization of brushless doubly fed machines with multibarrier rotors. *IEEE Trans. Ind. Appl*., 2019, 55(6): 5758-5767.

Peng Han received the B.Sc. and Ph.D. degrees in Electrical Engineering from the School of Electrical Engineering, Southeast University, Nanjing, China, in 2012 and 2017, respectively.

From November 2014 to November 2015, he was a joint Ph.D. student funded by China Scholarship Council with the Department of Energy Technology, Aalborg University, Aalborg, Denmark, where he focused on the brushless doubly-fed machines for wind energy conversion and high power drive. He was a Postdoctoral Researcher with the Center for High Performance Power Electronics (CHPPE), Department of Electrical and Computer Engineering, The Ohio State University, and later the SPARK Laboratory, Department of Electrical and Computer Engineering, University of Kentucky. He is currently with Ansys, Inc. as an Application Engineer. His current research interests include electric machines, power electronics and renewable energy.

Ming Cheng received the B.Sc. and M.Sc. degrees from the department of Electrical Engineering, Southeast University, Nanjing, China, in 1982 and 1987, respectively, and the Ph.D. degree from the Department of Electrical and Electronic Engineering, University of Hong Kong, Hong Kong, China, in 2001, all in Electrical Engineering.

Since 1987, he has been with Southeast University, where he is currently a Chief Professor at the School of Electrical Engineering and the Director of the Research Center for Wind Power Generation. From January to April 2011, he was a Visiting Professor with the Wisconsin Electric Machine and Power Electronics Consortium (WEMPEC), University of Wisconsin, Madison, WI, USA. His teaching and research interests include electrical machines, motor drives for EV, and renewable energy generation. He has authored or co-authored more than 400 technical papers and 5 books, and is the holder of 130 patents in these areas.

Prof. Cheng is a Fellow of the Institute of Electrical and Electronics Engineers, and a Fellow of the Institution of Engineering and Technology. He has served as the Chair and an Organizing

Committee Member for many international conferences. He is a Distinguished Lecturer of the IEEE Industry Application Society in 2015/2016.

Xinkai Zhu received the B.Sc. degree from the School of Electrical Engineering, Shenyang University of Technology, Shenyang, China, in 2015, and the Ph.D. degree from the School of Electrical Engineering, Southeast University, Nanjing, China, in 2021, all in Electrical Engineering.

From January 2019 to January 2020, he was a Guest Ph.D. student funded by China Scholarship Council with the Center for Electric Power and Energy, Technical University of Denmark, Copenhagen, Denmark, where he focused on AC loss calculation and quench analysis of superconducting coils applied in wind power generators. He is currently a Lecturer with the Department of Electric Power Engineering, North China Electric Power University. His current research interests include design and analysis of superconducting electrical machines and wind power generation systems.

Zhe Chen received the B.Eng. and M.Sc. degrees in Power System and Automation from the Northeast China Institute of Electric Power Engineering, Jilin, China, in 1982 and 1986, respectively, and the Ph.D. degree in Power and Control from the University of Durham, Durham, UK, in 1997.

He is a Full Professor with the Department of Energy Technology, Aalborg University, Denmark. He is the Leader of Wind Power System Research Program with the Department of Energy Technology, Aalborg University and the Danish Principal Investigator for Wind Energy of Sino-Danish Centre for Education and Research. He has led many research projects and has more than 400 publications in his technical field. His research interests include power systems, power electronics, and electric machines; and his main current research interests include wind energy and modern power systems.

Dr. Chen is an editor of the IEEE Transactions on Power Systems, an Associate Editor of the IEEE Transactions on Power Electronics, a Fellow of the Institute of Electrical and Electronics Engineers, a Fellow of the Institution of Engineering and Technology, London, UK, a Chartered Engineer in the UK.